ELSEVIER

Chemical Physics 261 (2000) 61–74

Chemical Physics

www.elsevier.nl/locate/chemphys

A comparison of neutron scattering studies and computer simulations of polymer melts

G.D. Smith [a,b,*], W. Paul [c], M. Monkenbusch [d], D. Richter [d]

[a] *Department of Materials Science and Engineering, University of Utah, 122 S. Central Campus Drive Rm. 304, Salt Lake City, UT 84112, USA*

[b] *Department of Chemical Engineering and Fuels Engineering, University of Utah, 122 S. Central Campus Drive Rm. 304, Salt Lake City, UT 84112, USA*

[c] *Institut für Physik, Johannes-Gutenberg Universität, 55099 Mainz, Germany*

[d] *Institut für Festkörperforschung, Forschungszentrum Jülich, 52425 Jülich, Germany*

Received 25 February 2000; in final form 22 May 2000

Abstract

Neutron scattering and computer simulations are powerful tools for studying structural and dynamical properties of condensed matter systems in general and of polymer melts in particular. When neutron scattering studies and quantitative atomistic molecular dynamics simulations of the same material are combined, synergy between the methods can result in exciting new insights into polymer melts not obtainable from either method separately. We present here an overview of our recent efforts to combine neutron scattering and atomistic simulations in the study of melt dynamics of polyethylene and polybutadiene. Looking at polymer segmental motion on a picosecond time scale, we show how atomistic simulations can be used to identify molecular motions giving rise to relaxation processes observed in experimental dynamic susceptibility spectra. Examining larger length and longer time scale polymer dynamics involving chain self-diffusion and overall conformational relaxation, we show how simulation results can motivate experiment and how combined results of scattering and simulation can be used to critically test theories that attempt to describe melt dynamics of short polymer chains.

1. Introduction

The dynamics of polymer melts cover an amazing range of time and length scales. The largest scales involve relaxation of entangled polymer chains, which, while becoming accessible to simulations using coarse-grained models, still cannot be simulated using detailed, quantitative models. However, modern workstations, parallel computers and efficient algorithms have made all time and length scales pertaining to the molecular dynamics of unentangled polymer chains in the melt accessible to atomistically detailed models [1–10]. With a sufficiently accurate potential describing intramolecular and intermolecular interactions for the polymer of interest, it is possible to investigate the molecular dynamics of short polymer chains on time scales from 1 fs up to 100 ns, or even, with sufficient patience, several μs. Access to molecular level information on polymer molecular dynamics covering nine orders of magnitude of time poses a serious challenge to experimentalists. Fortunately,

* Corresponding author. Fax: +1-801-581-4816.

E-mail address: gsmith2@geoffrey.emro.utha.edu (G.D. Smith).

0301-0104/00/$ - see front matter
PII: S0301-0104(00)00228-7

neutron scattering techniques are capable of covering much of this range. Improvements in neutron spin echo (NSE) spectroscopy have made measurement of melt dynamics on length scales up to 200 Å and time scales up to 200 ns possible. In the past decade, NSE studies of chain dynamics ranging from Rouse dynamics of short chains [9,11,12] to the Rouse/repetation crossover regime [13–15], to investigation of fully entangled chains and their dynamics [16] have been conducted. The much more local segmental dynamics in polymer melts have been the focus of both NSE and neutron time-of-flight (TOF) measurements [7,12,17–27]. These studies have been motivated by fundamental interest in the relationship between segmental dynamics and relaxation processes in polymers, as well as the desire to obtain experimental data to test various theories for these processes.

Below, we describe our efforts to combine atomistic molecular dynamics simulations and neutron scattering to gain new insight into polymer melt dynamics and to critically test the widely used theoretical models for the dynamics of unentangled polymer melts. The latter also forms the basis for theoretical models of entangled polymers. In Section 2, we consider segmental dynamics in polyethylene (PE) as measured by incoherent TOF neutron scattering, and discuss what these measurements and concomitant atomistic simulations can tell us about the mechanisms of relaxations in polymer melts on the picosecond time scale. In Section 3, we consider longer time and larger length scales, relevant to chain self-diffusion and overall conformational relaxation. Here, the single chain dynamic structure factor as obtained from NSE measurements and atomistic simulations are compared for polybutadiene (PBD) melts. A critical examination of the Rouse model and related theoretical treatments of polymer melt dynamics is carried out, and the shortcomings of these models are discussed.

2. Small-scale dynamics

In this section, we look at segmental motion in a melt of the *n*-alkane $C_{100}H_{202}$, corresponding to a PE chain below the entanglement molecular weight, at 509 K. Neutron scattering experiments [7] were performed on a hydrogenous PE sample using the time focusing TOF spectrometer IN6 at the Institut Laue-Langevin in Grenoble. The incoherent dynamic structure factor $S_{\rm inc}(q,\omega)$ was obtained for six momentum transfers ranging from $q = 0.8$ Å^{-1} to $q = 1.8$ Å^{-1}. Molecular dynamics simulations [6,7] were performed on a system of 40 $C_{100}H_{202}$ chains in a cubic simulation cell at experimental density (linear size ≈ 50 Å). These NVT simulations were conducted using the extended ensemble constant temperature algorithm of Nosé [28] using a 1 fs time step. Periodic boundary conditions were employed. Simulations were carried out using both an explicit atom (EA) model for PE as well as a united atom (UA) model, where CH_2 and CH_3 groups were represented by a single Lennard-Jones force center with the appropriate group mass. For the UA simulations, 9 ns of sampling followed approximately the same amount of equilibration. For the EA simulations, final UA configurations were equilibrated for 200 ps after placement of hydrogen atoms followed by 1.1 ns of sampling.

While the TOF measurements yield the measured incoherent dynamic structure factor $S^{\rm m}_{\rm inc}(q,\omega)$ in the frequency domain, molecular dynamics simulations yield dynamical information in the time domain. The intermediate incoherent dynamic structure $S_{\rm inc}(q,t)$ can be obtained directly from simulation. Beginning with the relationship [29]

$$S_{\rm inc}(q,t) = \frac{1}{N}\sum_{m=1}^{N}\langle \exp[{\rm i}\boldsymbol{q}\cdot\Delta\boldsymbol{R}_m(t)]\rangle, \tag{1}$$

where $\Delta\boldsymbol{R}_m(t) = \boldsymbol{R}_m(t) - \boldsymbol{R}_m(0)$, the displacement of scattering center m after time t, and the sum is over all N (assumed identical) scattering centers. When the sample is isotropic, as in the melt, Eq. (1) can be simplified to [29]

$$S_{\rm inc}(q,t) = \sum_{m=1}^{N}\langle \sin[q\,\Delta R_m(t)]/q\,\Delta R_m(t)\rangle, \tag{2}$$

where $\Delta R_m(t)$ is the magnitude of $\Delta\boldsymbol{R}_m(t)$. It is this latter relationship that we employ in calculating

$S_{inc}(q,t)$ from simulation. Because of the small incoherent scattering length of carbon atoms, the observed scattering is due almost entirely to the hydrogen atoms. Therefore, the summation is done over all hydrogen atoms in the system. For the UA model, we reinsert the hydrogen atoms into a stored time series of configurations (molecular dynamics trajectory) at their mechanical equilibrium positions in order to calculate $S_{inc}(q,t)$. Experimentally, the measured incoherent dynamic structure factor $S^{m}_{inc}(q,\omega)$ is a convolution of $S_{inc}(q,\omega)$ and the resolution function $R(\omega)$, which is measured separately. After Fourier transformation of $S^{m}_{inc}(q,\omega)$ and $R(\omega)$ to the time domain, the deconvolution becomes

$$S_{inc}(q,t) = S^{m}_{inc}(q,t)/R(t). \quad (3)$$

Therefore, $S_{inc}(q,\omega)$ is obtained in both TOF experiment and simulation by Fourier transforming $S_{inc}(q,t)$ into the frequency domain.

2.1. Comparison of experiment and simulation

Fig. 1 shows the dynamic susceptibility $\chi(q,\omega) = \omega S_{inc}(q,\omega)$ for a momentum transfer of $q = 1.8$ Å^{-1} obtained for PE from both TOF neutron scattering measurements and molecular dynamics simulations. The main relaxation peak in the susceptibility is nicely reproduced by both the EA and UA simulation models, both in position and in width. Quantitatively, the EA simulation is in better agreement with the experiment. The vertical bar indicates the maximum frequency (energy transfer) for the experiment at this momentum transfer. The experimental curve at higher frequencies is obtained from a power law extrapolation of the high frequency wing of $S^{m}_{inc}(q,\omega)$. The higher maximum value of $\chi(q,\omega)$ obtained from experiment as compared to simulation is due to the fact that the experimental extrapolation procedure underestimates the high frequency contribution to the relaxation process.

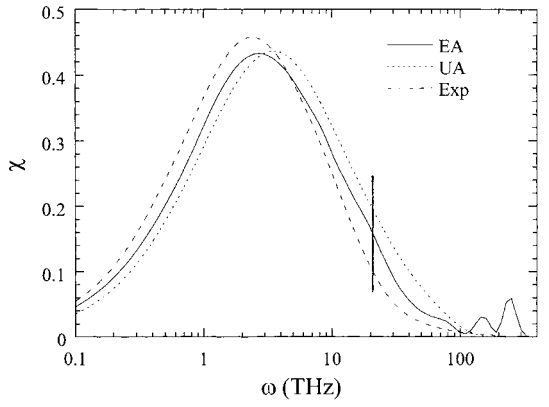

Fig. 1. Dynamic susceptibility of a PE melt at 509 K as determined from TOF neutron scattering (EXP), explicit atom (EA) molecular dynamics simulations and united atom (UA) molecular dynamics simulations for $q = 1.8$ Å^{-1}. The vertical line shows approximately the upper frequency limit of the experiment.

The EA simulation clearly displays high frequency peaks around 150 and 250 THz that are due to C–C–H and H–C–H bond angle vibrations (the C–H and C–C bond lengths are kept fixed in the simulation). These peaks are absent in the experiment because they are outside the experimental frequency window and are absent in the UA simulation because these degrees of freedom have been eliminated in the UA representation. As a consequence, both the experiment and UA simulation are unable to resolve the motion of the hydrogen atoms on very short time scales (high frequencies). This is further exemplified in Fig. 2 where we have used the Gaussian approximation for the self part of the van Hove function to relate the incoherent scattering function to the mean-square displacement of the hydrogen atoms [30]

$$\langle \Delta R^2_m(t) \rangle = -6 \ln [S_{inc}(q,t)]/q^2, \quad (4)$$

where $\langle \Delta R^2_m(t) \rangle$ is the mean-square displacement of the scattering centers (hydrogen atoms) after time t. If the Gaussian approximation of the van Hove function is correct, the predicted mean-square displacements from Eq. (4) should coincide for all employed scattering vectors. The mean-square displacement curves obtained from $S_{inc}(q,t)$ for the EA simulation for all momentum transfers between $q = 0.8$ Å^{-1} and $q = 1.8$ Å^{-1} (upper solid line(s) in Fig. 2) indeed superimpose on the subpicosecond time scale. The hydrogen atom displacement shows an oscillatory contribution on these time scales due to the bond angle vibrations,

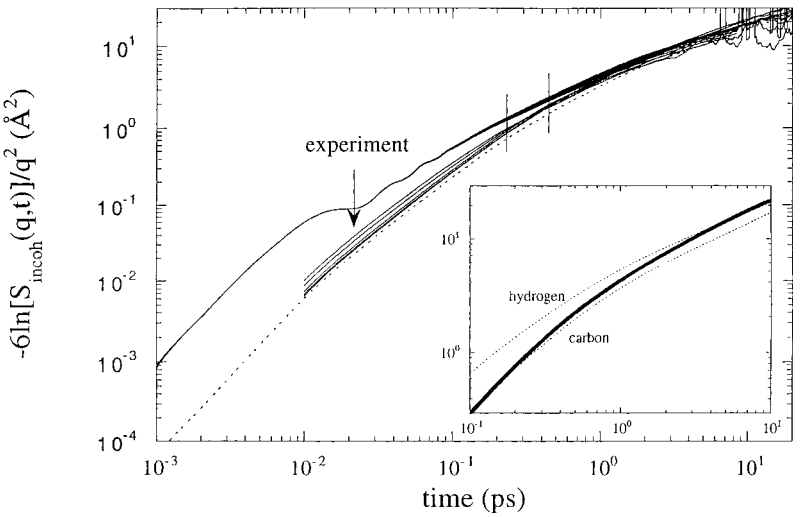

Fig. 2. Mean-square hydrogen displacements obtained directly or via Eq. (4) from TOF neutron scattering experiments and EA molecular dynamics simulations for a PE melt at 509 K. The dashed line is for carbon atoms for simulations. The vertical lines show the lower time limits for the experimental data for the lowest and highest momentum transfers as determined from Nyquist angular frequencies ($t_{\min} = \pi/\omega$). The inset shows longer time behavior from simulation (- - -) and experiment at $q = 0.8$ Å^{-1} (—).

which is neither seen in the carbon displacements (dashed line) nor in the experimental predictions for the hydrogen atom displacement (splayed set of solid curves obtained from applying Eq. (4) to the experimental $S_{\text{inc}}(q,t)$). The experimental curves follow the hydrogen displacement curve from simulation at times larger than a few picoseconds. For shorter times (lying outside the experimental time windows indicated by the vertical bars), the extrapolated displacement from experiment traces the backbone motion since the high frequency bending motions are not seen experimentally. Due to the error from extrapolation, the experimental, curves do not superimpose as perfectly as the simulation data. The inset in Fig. 2 shows the crossover in the experimental data from tracing the hydrogen displacement to tracing the backbone displacement in more detail.

2.2. Relaxation mechanisms

Having clearly shown that atomistic molecular dynamics simulations accurately reproduce molecular dynamics in the PE melt on the picosecond time scale, we can now attempt to discern exactly what molecular motions give rise to the main relaxation peak shown in Fig. 1. There are two prime candidates for this: librational motion in the *trans* and *gauche* minima of the backbone dihedral potentials and transitions between these minima (conformational transitions). From spectra at 509 K, it is not possible to resolve which motions make the most important contribution to the observed peak because the librations and transitions occur on a similar time (frequency) scale. The processes should, however, differ significantly in their temperature dependence. The librational frequencies should be independent of temperature as long as the motion is approximately harmonic, whereas the transition rate between the minima in the dihedral potential typically displays a strong Arrhenius temperature dependence. Lowering the temperature should therefore separate these two contributions along the frequency axis in experiment as well as simulation, moving transitional contributions to lower frequency. In the simulation, we can generate similar behavior by modifying the dihedral potential function. Increasing the barriers between the torsional minima by a factor of two has an exponential effect on the

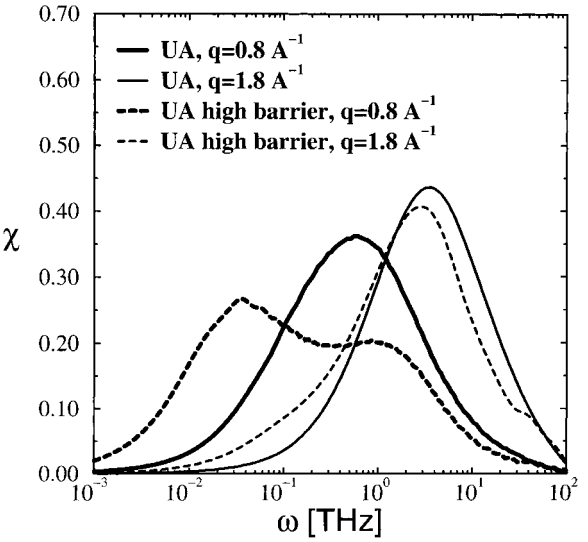

Fig. 3. Dynamic susceptibility for a PE melt at 509 K from molecular dynamics simulation using the original UA potential and a UA potential with an increased rotational energy barrier.

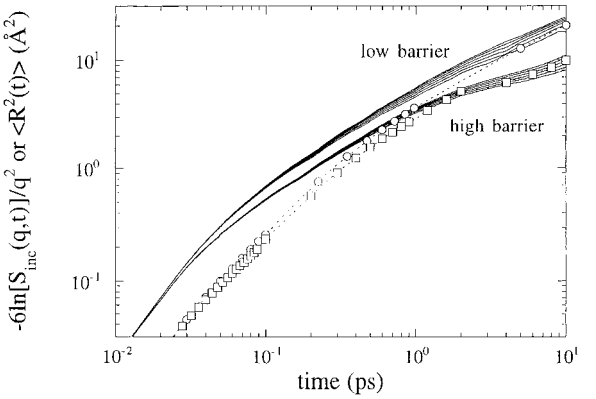

Fig. 4. Mean-square hydrogen displacements (lines, from Eq. (4)) for a PE melt at 509 K obtained from UA simulations. The symbols show carbon displacements from the original UA potential (○) and the high barrier model (□).

transition rate but slightly *increases* the libration frequencies due to the increased curvature of the potential in the dihedral minima.

Fig. 3 shows a comparison of the susceptibility spectra for $q = 0.8$ Å^{-1} and $q = 1.8$ Å^{-1} for the original potential and the potential with increased barriers. We can see that the type of motion that makes the most important contribution to the susceptibility peak depends on the length scale of observation. For a momentum transfer of $q = 1.8$ Å^{-1}, where we probe motions on a length scale of 3–4 Å, the spectrum shows little change when the barriers are increased. Hence, for motions on this length scale, the main contribution comes from librations. For $q = 0.8$ Å^{-1}, where we are probing motions on the scale of 8 Å, librations and transitions contribute about equally and are clearly separated when we increase the torsional barriers. Specifically, the low frequency peak for the modified potential is generated by torsional transitions and shifted by about a factor of 20 to lower frequencies compared to the original potential.

When we look at the mean-square displacement of hydrogen atoms and backbone carbons displayed in Fig. 4 in a comparison between the original and the modified potential, we can identify the time scale at which torsional transitions of the backbone angles start to contribute to the translational motion of the atoms. We know from an analysis of the torsional transitions with the original potential that the mean time between transitions is approximately 7 ps. The fact that the high and low barrier displacements differ down to sub-picosecond time scales tells us that the distribution of conformational transition times extends into this time regime for the original potential. Around 1 ps, these transitions become the dominant type of motion in generating particle displacement. In contrast, at around 1 ps, the mean-square displacements in the high barrier model develop a plateau region extending to about 10 ps indicating that vibrations and librations have saturated and torsional transitions are not yet significant. For the modified potential, the mean time between torsional transitions is of the order of 100 ps. Here, the distribution of transition times extends down to around 1 ps, with the upturn of the mean-square displacement curve in the modified potential around 10 ps marking the crossover to torsional transition-dominated displacement. We also remark that the time scale on which the superposition of the mean-square displacement predictions for different momentum transfers starts to fail coincides closely with the onset of torsional transitions. These anharmonic motions do not

fulfill the dynamic Gaussian assumption for the van Hove function which underlies this figure.

2.3. Conclusions

In this section, we give an example of the synergy that is possible between experiment and simulation in clarifying mechanisms underlying features in the relaxation spectrum for a polymer melt on the picosecond time scale. First, it was found necessary to demonstrate that atomistic simulations using accurate potential functions are capable of reproducing the dynamics of polymer melts on this time scale. The flexibility of the simulations then allowed us to separate motions in the time/frequency window of the relaxation process we wanted to understand by judicially modifying the potential function. Specifically, this approach has allowed us to disentangle the contributions from torsional librations and torsional transitions to the broad susceptibility maximum seen in incoherent scattering from PE melts. We have shown that the relative contributions of these two types of motion to the relaxation peak depend on the length scale studied, i.e. the momentum transfer employed in the scattering. Librational motions are dominant on small length scales, whereas the torsional transitions are more important on length scale of several backbone bonds.

3. Large-scale polymer chain dynamics

Neutrons can also be used to probe larger length scale dynamics of polymer chains. NSE techniques allow measurement of the single chain dynamic structure factor on length scales much larger than the radius of gyration (R_g) of unentangled chains down to length scales of the order of R_g for these chains on a time scale ranging from 50 ps up to 200 ns. The technique yields the structure factor directly in the time domain, simplifying comparison with simulations. The single chain intermediate coherent dynamic structure factor measured in NSE experiments corresponds to [29]

$$S'(q,t) = \sum_{(m,n)} \langle \exp[i\boldsymbol{q}\cdot(\boldsymbol{R}_m(t) - \boldsymbol{R}_n(0))]\rangle \Big/ \sum_{(m,n)} \langle \exp[i\boldsymbol{q}\cdot(\boldsymbol{R}_m(0) - \boldsymbol{R}_n(0))]\rangle, \quad (5)$$

where $\boldsymbol{R}_m(t) - \boldsymbol{R}_n(0)$ is the displacement vector between scattering centers m and n at time t with m and n belonging to the same chain. For an isotropic (melt) sample, this reduces to

$$S'(q,t) = \sum_{(m,n)} \langle \sin[qR_{mn}(t)]/qR_{mn}(t)\rangle \Big/ \sum_{(m,n)} \langle \sin[qR_{mn}(0)]/qR_{mn}(0)\rangle, \quad (6)$$

where $R_{mn}(t)$ is the magnitude of $\boldsymbol{R}_m(t) - \boldsymbol{R}_n(0)$. When $q \ll 2\pi/R_g$, one can observe only the overall motion of the chain molecules, and assuming the center of mass motion is diffusive:

$$S'(q,t) = \exp(-q^2\langle R_{cm}(t)^2\rangle/6) = \exp(-q^2 D_{cm} t), \quad (7)$$

where $\langle R_{cm}(t)^2\rangle$ is the mean-square center of mass displacement of the chains and D_{cm} is their center of mass self-diffusion coefficient. From molecular dynamics simulations, both $S'(q,t)$ and D_{cm} can be determined directly from the trajectories and compared with experiment.

3.1. Comparison of experiment and simulation

Recently, NSE measurements were performed on an unentangled PBD melt [12]. The microstructure of the chains was 40% 1,4-*cis*, 50% 1,4-*trans* and 10% 1,2-vinyl units. The *z*-average chain microstructure is represented by a chain of 30 repeat units, three of which are 1,2-vinyl units, with a molecular weight of 1622 Da. This average chain has 114 backbone carbon atoms. The NSE measurements were performed on the NSE spectrometer at the FRJ-2 reactor in Jülich. A deuterated matrix containing 12% protonated material was used. Using a neutron wavelength of $\lambda = 8.0$ Å, a dynamic range from 100 ps to 22 ns was covered. The experiments were performed at 353 K study-

ing spectra at seven different momentum transfers ($q = 0.05, 0.08, 0.10, 0.14, 0.20, 0.24$ and 0.30 Å^{-1}). The experimental background and the background from a deuterated matrix were obtained from separate spin echo measurements on a fully deuterated material and subtracted with the proper transmission factors.

We also performed molecular dynamics simulations of the PBD melt [12,31]. Intramolecular and intermolecular interactions were described using a UA potential function parametrized to accurately reproduce the conformational energetics of model compounds as determined from high-level quantum chemistry calculations. We generated a random copolymer system of 40 chains each comprised of 30 units with a microstructure of 40%/50%/10% *cis*/*trans*/vinyl units. Hence, each chain contains three vinyl units and 114 backbone carbons. These chains have a molecular weight of 1622 Da, in agreement with the $M_z = 1600$ Da of the synthesized chains. Periodic boundary conditions were employed and the SHAKE algorithm was used to constrain bond lengths. A reversible multiple-time-step algorithm was employed [32] with an inner time step of 1 fs for bonded interactions and an outer time step of 5 fs for nonbonded interactions. Following 10 ns of equilibration, a 40 ns constant volume trajectory was generated. The single chain dynamic structure factor $S'(q,t)$ was subsequently determined from the stored trajectory using Eq. (6).

$S'(q,t)$ from NSE measurements and simulation for PBD at 353 K are shown in Fig. 5. Application of Eq. (7) to the $q = 0.05$, 0.08 and 0.010 Å^{-1} data yields $D_{cm} = 2.7 \times 10^{-7}$ cm^2/s for experiment and $D_{cm} = 3.6 \times 10^{-7}$ cm^2/s for simulation. We can compensate for the small difference (a difference of 25% in the self-diffusion coefficient between experiment and simulation reflects excellent agreement) in the center of mass diffusion rate between simulation and experiment through scaling of the experimental times by a factor of 0.75. This is shown in Fig. 5. Excellent agreement is seen between experiment and simulation. It is possible to calculate an apparent mean-square center of mass displacement of the chains from the dynamic structure factor. Rearrangement of Eq. (7) yields

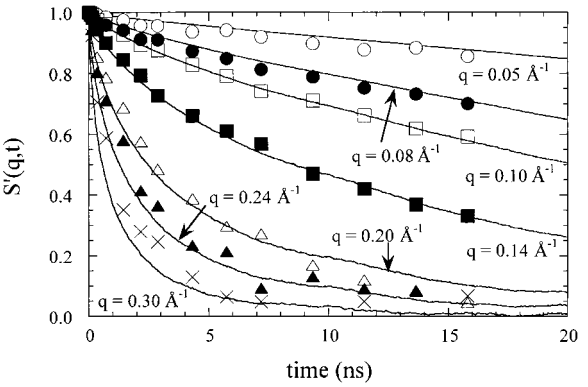

Fig. 5. Dynamic structure factor for PBD chains obtained from simulation (lines) and neutron spin echo measurements (symbols).

$$\langle R_{cm}(t)^2 \rangle_{app} = \frac{-6 \ln [S'(q,t)]}{q^2}, \tag{8}$$

where $\langle R_{cm}(t)^2 \rangle_{app}$ indicates an apparent mean-square center of mass displacement, since Eq. (8) yields the true center of mass displacement only in the limit $q \ll 2\pi/R_g$. $\langle R_{cm}(t)^2 \rangle_{app}$ obtained from application of Eq. (8) to experimental $S'(q,t)$ data for $q = 0.05$, 0.08 and 0.10 Å^{-1} is shown in Fig. 6 along with $\langle R_{cm}(t)^2 \rangle$ obtained directly from simulation. Also shown is $\langle R_{cm}(t)^2 \rangle$ obtained from Eq. (7) using the polymer self-diffusion coefficient obtained from simulation. For times longer than the

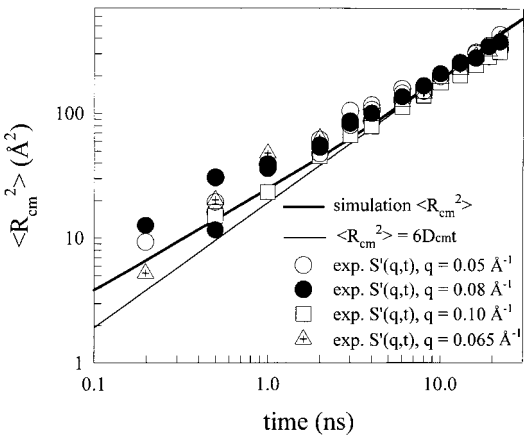

Fig. 6. Mean-square center of mass displacement of PBD chains.

chain Rouse time $\tau_R = 15$ ns (see later), the center of mass motion is clearly diffusive and is well described by Eq. (7). However, for times less than τ_R, the motion is sub-diffusive. In this time regime, the mean-square center of mass motion is well described by a power law relationship $\langle R_{cm}(t)^2 \rangle \sim t^a$ where $a \approx 0.8$. Similar sub-diffusive behavior has been observed in other atomistic [9] and coarse-grained polymer simulations [33,34] for $t < \tau_R$. A recent theoretical study also found that interactions of a chain in the melt with $\sqrt{N}$ other chains leads to sub-diffusive behavior for times less than τ_R [35]. The sub-diffusive behavior seen in the molecular dynamics simulations of the PBD melt motivated additional NSE experiments on the melt at short times. The $\langle R_{cm}(t)^2 \rangle_{app}$ data obtained from these NSE measurements of PBD (Fig. 6) are the first experimental confirmation of sub-diffusive behavior in polymer melts for $t < \tau_R$.

3.2. Theoretical models

3.2.1. The Rouse model

The excellent agreement observed between simulation and experiment for $S'(q,t)$ (Fig. 5) allows us to investigate in detail the validity of various theoretical models for polymer melt dynamics by comparing predictions of these models with simulation. The best known and most widely employed model for polymer melt dynamics is the Rouse model [29,36]. In the Rouse model, the polymer chain is treated as a set of beads, each connected to its immediately preceding and following neighbor by harmonic springs. Excluded volume and hydrodynamic interactions are disregarded. The spring force constant is $k = 3k_BT/b^2$, where b^2 is the mean-square length of a segment. The segments are subjected to Gaussian random (Brownian) forces and frictional drag forces characterized by a segmental friction coefficient ζ. Solution of the resulting equation of motion yields [29]

$$\langle R^2 \rangle = Nb^2, \tag{9}$$

where $\langle R^2 \rangle$ is the mean-square end-to-end distance of the chain and N is the number of bonds, which, for a Rouse chain, is equal to the number of Kuhn segments, and [29]

$$D_{cm} = \frac{k_BT}{N\zeta}. \tag{10}$$

Hence, the force constant and segmental friction coefficient are established by the chain dimensions and center-of-mass motion of the chains, respectively. The latter is predicted to be diffusive in the Rouse model. The Rouse model has no other adjustable parameters. The solution of the Rouse equation of motion is determined analytically by transformation to its eigenmodes, the Rouse modes, which are defined as [6]

$$\boldsymbol{X}_p(t) = \frac{1}{N}\sum_{n=1}^{N} \cos\left(p\pi\frac{n-1/2}{N}\right)\boldsymbol{R}_n(t), \tag{11}$$

where p is the mode index ($1 \leqslant p \leqslant N$) and $\boldsymbol{R}_n(t)$ is the Cartesian coordinates of segment n. For the Rouse modes, the model yields the self-correlation function [29]

$$\langle \boldsymbol{X}_p(t) \cdot \boldsymbol{X}_p(0) \rangle = \frac{\langle R^2 \rangle}{2\pi^2 p^2} \exp[-p^2 t/\tau_R], \tag{12}$$

where for PBD at 353 K, the Rouse time $\tau_R = \langle R^2 \rangle/(3\pi^2 D_{cm}) = 15.0$ ns using $\langle R^2 \rangle$ and D_{cm} from simulation. The Rouse model yields a Gaussian distribution of all intersegmental displacements $\boldsymbol{R}_m(t) - \boldsymbol{R}_n(0)$. This, and the fact that $\langle \boldsymbol{X}_r(t) \cdot \boldsymbol{X}_s(t) \rangle = 0$ for $r \neq s$, allows calculation of the dynamic structure factor for Rouse chains using the expression [29]

$$\begin{aligned} S'(q,t) = \frac{1}{N}\exp\{-q^2 D_{cm} t\} \\ \times \sum_{(m,n=1)}^{N} \exp\left\{-\frac{q^2\langle R^2\rangle}{6N}|n-m| - \frac{2q^2\langle R^2\rangle}{3\pi^2}\right. \\ \times \sum_{p=1}^{N}\frac{1}{p^2}\cos\left(\frac{p\pi n}{N}\right)\cos\left(\frac{p\pi m}{N}\right) \\ \left. \times \left[1 - \exp(-tp^2/\tau_R)\right]\right\}. \end{aligned} \tag{13}$$

A comparison of $S'(q,t)$ from simulation and the Rouse predictions (Eq. (13)) is shown in Fig. 7.

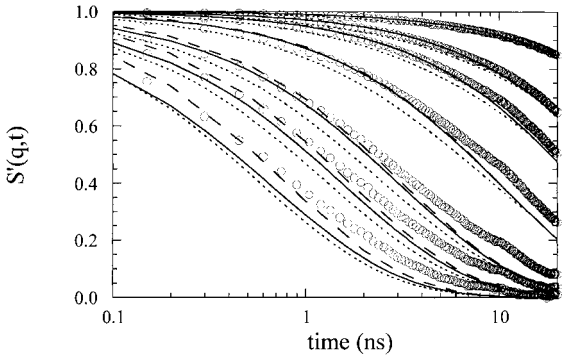

Fig. 7. Dynamic structure factor for PBD chains obtained from simulation (○), the Rouse model (—), the modified Rouse model (···), and the SFCM (– – –).

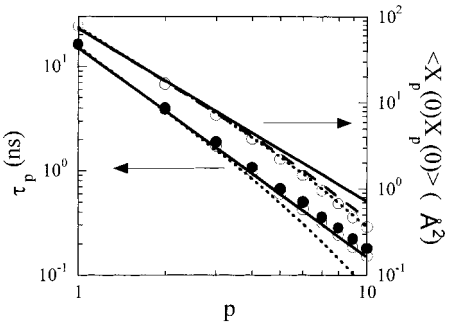

Fig. 8. Normal mode amplitude and relaxation time for PBD chains from simulation (symbols, with filled circles being correlation times), the Rouse model (—), the SFCM (···) and the internal viscosity model (– – –).

Consistent with comparisons of the Rouse model with simulations of coarse-grained lattice models [37–40], of bead-spring polymer models [41], and of recent simulations of atomistic models [9], the Rouse model does a poor job in reproducing the dynamic structure factor, particularly for larger q values and longer times.

A detailed analysis of the simulation trajectories allows us to investigate in detail the fundamental predictions of the Rouse model. We start by calculating the Rouse modes from the simulation by employing Eq. (11), where the sum is now performed over all hydrogen atoms of the chain and the average is performed over the 40 ns simulation trajectory. From Eq. (12), the amplitude of the pth mode is expected to scale as p^{-2}, specifically, $\langle \boldsymbol{X}_p(0) \cdot \boldsymbol{X}_p(0) \rangle = \langle R^2 \rangle / (2\pi^2 p^2)$. The amplitudes for the Rouse modes as predicted by the Rouse model and as determined from simulation are compared in Fig. 8. Modes $p > 10$ do not contribute to $S'(q,t)$ for the range of q values investigated. Due to chain stiffness, the amplitudes for modes $p > 3$ begin to show deviation from Rouse predictions as the distances are no longer Gaussian distributed. The relaxation time for the self-correlation function (Eq. (12)) of a mode is also expected to scale as p^{-2}, specifically, $\tau_p = \tau_R / p^2$. The relaxation times, as predicted by the Rouse model and as determined from simulation, are also shown in Fig. 8. The mode self-correlation functions from simulation do not show single exponential decay as predicted by Eq. (12), but are well represented by a stretched exponential

$$\langle \boldsymbol{X}_p(t) \cdot \boldsymbol{X}_p(0) \rangle = \langle \boldsymbol{X}_p(0) \cdot \boldsymbol{X}_p(0) \rangle \exp[-(t/\tau_p)^{\beta}], \tag{14}$$

where β ranges from 1.0 for $p = 1$ to 0.75 for $p = 10$. Values of τ_p determined from fitting Eq. (14) to the mode self-correlation functions and the corresponding correlation times, given as the time integral of $\exp[-(t/\tau_p)^{\beta}]$, are shown in Fig. 8. The larger p modes begin to show some slowing, relative to Rouse predictions, but the difference is small for modes contributing to $S'(q,t)$ for the q range investigated. In the Rouse model, the relaxation times are proportional to the mode amplitudes. This scaling is clearly not followed for the real chains, as the relaxation times are actually somewhat longer than the Rouse predictions, while the mode amplitudes are smaller. In the internal viscosity model, local friction effects can allow for relaxation times longer than Rouse predictions despite reduced mode amplitudes.

In order to investigate the influence of reduced mode amplitudes, increased relaxation times, and sub-diffusive center of mass motion on the predicted $S'(q,t)$, we modified Eq. (13) to include these effects, yielding

$$S'(q,t) = \frac{1}{N}\exp\left\{ -q^2\frac{\langle R_{\rm cm}(t)^2\rangle}{6}\right\} \times \sum_{(n,m=1)}^{N}\exp\left\{ -\frac{q^2\langle R^2\rangle}{6N}|n-m| - \sum_{p=1}^{N}\frac{4\langle \boldsymbol{X}_p(0)\cdot\boldsymbol{X}_p(0)\rangle}{3} \times \cos\left(\frac{p\pi n}{N}\right)\cos\left(\frac{p\pi m}{N}\right) \times \left[1-\exp\left(-(t/\tau_p)^{\beta}\right)\right]\right\}, \quad (15)$$

where the mean-square center of mass displacement $\langle R_{\rm cm}(t)^2\rangle$, mode amplitudes $\langle \boldsymbol{X}_p(0)\cdot\boldsymbol{X}_p(0)\rangle$ as well as relaxation times τ_p and stretching exponents β are taken from simulation. The resulting dynamic structure factor is shown in Fig. 7. $S'(q,t)$ decays faster than predicted by the Rouse model and is actually in somewhat poorer agreement with $S'(q,t)$ from simulation than the Rouse predictions. The faster decay is due to the fact that $\langle R_{\rm cm}(t)^2\rangle$ is greater in the sub-diffusive regime than predicted by the Rouse model (see Fig. 6). The predictions of Eq. (15) and those of the Rouse model (Eq. (13)) merge at the Rouse time, where the center of mass displacement is well described by the Rouse model. Neglecting sub-diffusive behavior (results not shown), Eq. (15) yields a slightly slower decay in $S'(q,t)$ compared to the Rouse model for larger q values, but does not significantly improve agreement with simulation. Clearly, incorporating differences in mode amplitudes and relaxation into the Rouse predicted scattering function is not sufficient to account for the large discrepancies observed in $S'(q,t)$. We will return to these issues after a brief discussion of related models intended to improve on the Rouse model.

3.2.2. Semi-flexible chain and internal viscosity models

Several models for polymer dynamics have been proposed that take into account local stiffness effects (non-Gaussian distance distributions on small length scales) on polymer dynamics not accounted for in the Rouse model. It has been claimed that a semi-flexible chain model (SFCM) [42,43] that accounts for the effects of chain stiffness on scales comparable to the persistence length does a much better job in reproducing experimental $S'(q,t)$ than the Rouse model. In addition to the center of mass diffusion coefficient, this model has two additional adjustable parameters; the contour length $L_{\rm c}$ and the persistence length $L_{\rm p}$. Using the relationships for a Kratky–Porod worm-like chain, it is possible, from the characteristic ratio of PBD as determined from simulation, to establish values of $L_{\rm p} = 5.0$ Å and $L_{\rm c} = 147$ Å. These parameters yield $\langle R^2\rangle/\langle R_{\rm g}^2\rangle = 1420$ Å^2 / 221 Å$^2 = 6.4$. From simulations, $\langle R^2\rangle/\langle R_{\rm g}^2\rangle = 1414$ Å^2/224 Å$^2 = 6.3$. Use of significantly stiffer semi-flexible chains as was done for PE in order to achieve the claimed good agreement of the model with experiment and simulation [43] does not reproduce the static structure of the chain on larger length scales.

Predictions of $S'(q,t)$ for the semi-flexible model with $L_{\rm p} = 5.0$ Å, $L_{\rm c} = 147$ Å and $D_{\rm cm} = 3.2\times10^{-7}$ cm^2/s are shown in Fig. 7. The corresponding mode amplitudes and relaxation times are given in Fig. 8. Mode amplitudes for $p \leqslant 10$ are in good agreement with those from simulation, and are reduced from the Rouse amplitudes, indicating the influence of local chain stiffness. The corresponding relaxation times, as with the Rouse model, are proportional to the mode amplitude, and hence are shorter than those predicted by the Rouse model, and are in poor agreement with simulation for larger p. The dynamic structure factor obtained from the SFCM shows little, if any, improvement in agreement with simulation over the Rouse model. At long times, predictions are indistinguishable from the Rouse predictions. At short times and large q values, the decay of $S'(q,t)$ from the semi-flexible model is significantly slower than that seen in the simulations. This may come partially from the reduced amplitudes of the larger p modes compared to the Rouse model. However, as the mode amplitudes from the semi-flexible model are similar to those from simulation, and the relaxation times are actually shorter than from simulation, the effect of amplitude reduction on $S'(q,t)$ cannot account for the majority of the re-

duced decay in $S'(q,t)$ at short time and large q seen with the semi-flexible model. This reduction, which becomes greater with increasing chain stiffness, must therefore be due to the non-Gaussian distribution of distances within the semi-flexible chain, and is discussed in detail below.

Another approach to including chain stiffness effects on dynamics has been proposed by Allegra and Ganazzoli [44,45] referred to as the internal viscosity model. In this approach, Rouse mode amplitudes are determined through application of the generalized characteristic ratio $C(q)$, which contains full information on the geometrical averages of the unperturbed chain. The resulting mode amplitudes for PBD are shown in Fig. 8 and are in good agreement with simulation and predictions of the SFCM. In addition to the inclusion of chain stiffness effects, the model includes internal viscosity effects, which can dramatically increase the relaxation times for the short wavelength normal modes compared to the corresponding times obtained from Rouse analysis. When the model was fit to experimental data for a polyisobutylene melt, a good description of $S'(q,t)$ was obtained [27]. Unlike polyisobutylene, a fit of the internal viscosity model to the PBD melt data does not yield a significant slowing down of short wavelength modes compared to that obtained from Rouse analysis. The internal viscosity model yields relaxation times somewhat slower than the SFCM and in good agreement with simulation. However, $S'(q,t)$ are found to be similar to those for the SFCM, indicating that the poor agreement between the Rouse (and the related models) and experiment for $S'(q,t)$ is not due to a slowing down of the normal modes.

3.3. Gaussian displacements and mode orthogonality

Summarizing what we have learned about chain dynamics in a PBD melt from comparison of experiment, simulation and theory, we conclude that (1) atomistic molecular dynamics simulations of unentangled polymer melts using quantum chemistry based potentials yield $S'(q,t)$ in excellent agreement with NSE measurements; (2) the Rouse model does a poor job in reproducing $S'(q,t)$ from simulation and experiment; (3) the failure of the Rouse model does not lie primarily in the predicted mode amplitudes or relaxation times; (4) efforts to improve upon the Rouse model by including local stiffness effects using the correct static structure of the chain do not lead to a significantly improved description of $S'(q,t)$; (5) phenomenologically inserting the sub-diffusive behavior of the center of mass displacement into the Rouse prediction for the scattering function does not account for the differences between theory and experiment/simulation. The question therefore remains as to why the models discussed here fail to accurately reproduce $S'(q,t)$.

Calculation of $S'(q,t)$ for these models is based on the assumptions that all segmental displacements $\boldsymbol{R}_m(t)-\boldsymbol{R}_n(0)$ are Gaussian distributed and that the eigenmodes remain orthogonal, i.e., $\langle \boldsymbol{X}_r(t)\cdot \boldsymbol{X}_s(0)\rangle = 0$ for $r \neq s$. Examination of cross-correlation for the $p \leqslant 4$ from simulation confirms that the modes remain orthogonal. Let us then consider the assumption of Gaussian distributed displacements. $S'(q,t)$ for isotropic systems is given by Eq. (6). Only when $\boldsymbol{R}_m(t)-\boldsymbol{R}_n(0)$ *are Gaussian distributed*, can the Gaussian approximation be invoked, allowing Eq. (6) to be recast as

$$S'(q,t) = \sum_{(m,n)} \exp\left[-q^2\langle R_{mn}(t)^2\rangle/6\right] \Big/ \sum_{(m,n)} \exp\left[-q^2\langle R_{mn}(0)^2\rangle/6\right]. \tag{16}$$

Since solution of the dynamic equation for each of the analytical model discussed above yields $\langle R_{mn}(t)^2\rangle$, Eq. (16) is conveniently employed in determining $S'(q,t)$. However, assumption of Gaussian distributed displacements is valid only for the Rouse model. Indeed, a primary goal of the SFCM and internal viscosity model is to account for the effects of chain stiffness on dynamics. Use of Eq. (16) is therefore only an approximation for all models considered here except the Rouse model.

We can get a picture of the influence of non-Gaussian distributed displacements on $S'(q,t)$ by using both Eqs. (6) and (16) for simulation chains, as shown in Fig. 9. $S'(q,t)$ yielded by Eq. (16) for

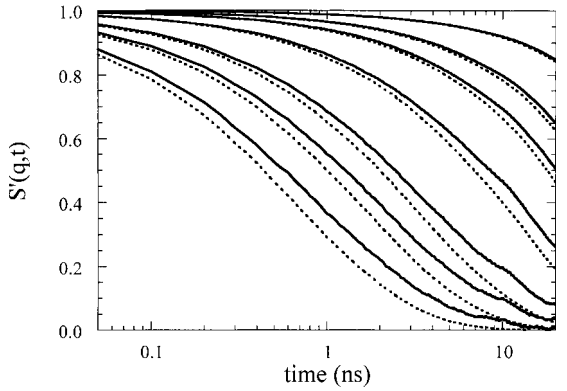

Fig. 9. Comparison of the dynamic structure factor for PBD chains obtained from simulation using Eq. (6) (—) and Eq. (16) (···).

the simulation chains are similar to the Rouse predictions. This indicates that the mean-square displacements on all time and length scales investigated are reasonably well described by the Rouse model, consistent with the reasonable agreement obtained between the Rouse model and simulations for normal mode amplitudes and relaxation times. In contrast, the variance in $S'(q,t)$ between the SFCM and simulation using Eq. (16) as well as the Rouse model at short times and larger q values indicates that the SFCM chain is too stiff on the corresponding length scales. However, we see in Fig. 7 that $S'(q,t)$ for the SFCM converges to the Rouse predictions after sufficient time. For the SFCM, all particle self-displacements $\boldsymbol{R}_m(t) - \boldsymbol{R}_m(0)$ are Gaussian distributed, so eventually $\boldsymbol{R}_m(t) - \boldsymbol{R}_n(0)$ and $S'(q,t)$ for the model converge with those for the Gaussian chain, i.e. the Rouse model. In contrast, $S'(q,t)$ from simulations using Eq. (6) do not converge with those from Eq. (16), even for $t \approx \tau_R$, clearly demonstrating that the displacements are not Gaussian distributed even on this time scale.

From the molecular dynamics trajectories, we can examine the displacement distributions as a function of $|n-m|$ and time. We find that even after τ_R, $\boldsymbol{R}_m(t) - \boldsymbol{R}_n(0)$ distributions show deviation from Gaussian behavior for all $|n-m|$. The influence of these non-Gaussian displacements on $S'(q,t)$ depends on q, t and $|n-m|$. However, non-Gaussian effects will in all cases slow the decay of $S'(q,t)$ relative to that obtained for a Gaussian distribution with the same mean-square displacements (e.g. see Fig. 9), consistent with the observed relationship between simulation and Rouse predictions. For example, the contribution of center of mass displacement to $S'(q,t)$ with the first non-Gaussian correction is given by [46]

$$S'_{cm}(q,t) = \exp[-q^2\langle R_{cm}(t)^2\rangle/6] \times [1 + 1/2[q^2\langle R_{cm}(t)^2\rangle/6]^2\alpha_2(t)], \quad (17)$$

where

$$\alpha_2(t) = \frac{3\langle R_{mn}(t)^4\rangle}{5\langle R_{mn}(t)^2\rangle^2} - 1. \quad (18)$$

For $t = 15$ ns and $q = 0.30$ Å^{-1}, simulations yield $\alpha_2(t) = 0.15$ and $1/2[q^2\langle R_{cm}(t)^2\rangle/6]^2\alpha_2(t) = 1.37$, clearly demonstrating the importance of non-Gaussian displacements. Non-Gaussian displacements for the center of mass and large $|n-m|$ after times comparable to τ_R can only result from non-diffusive behavior of the center of mass displacement and long wavelength modes such as the rotational diffusion of the molecule. Non-diffusive behavior for these modes results from intermolecular correlations, which are not included in any of the models considered except simulations.

3.4. Conclusions

We have demonstrated that molecular dynamics simulations using an accurate potential function can reproduce polymer melt dynamics on much longer time and larger length scales than those determined directly by conformational motions. Here, detailed analysis of the molecular dynamics of the melt from simulations motivated additional NSE measurements that provided the first experimental confirmation of sub-diffusive behavior in polymer melts. Comparison of the dynamic structure factor obtained from simulation and experiment with prediction of simple analytical theories shows significant deviations. Detailed analysis of the simulations and comparison with

model predictions reveals that it is primarily the non-Gaussian self-displacements $\boldsymbol{R}_m(t) - \boldsymbol{R}_m(0)$ resulting from intermolecular correlations that account for the deviation of Rouse predictions from simulation. Inclusion of chain stiffness does not significantly improve agreement with experiment.

We have given two examples of the synergism that is possible between neutron scattering and molecular simulations in the investigation of polymer melt dynamics. In the case of conformational dynamics, TOF measurements provided data whose mechanistic interpretation was greatly assisted by molecular simulations. In the case of chain dynamics, behavior that deviates from that predicted by widely used theoretical models was seen in the molecular simulations, motivating additional experiments that confirmed this behavior. We foresee that this type of interaction between neutron scattering experiments and atomistic simulations will be of increasing importance in the future aiding identification of mechanisms of molecular motion in dense polymer systems. This will be particularly true for systems with much more complex morphologies and dynamics such as entangled polymers, copolymers, blends, confined melts, and nanocomposites.

References

[1] R.J. Roe (Ed.), Computer Simulation of Polymers, Prentice Hall, Englewood Cliffs, NJ, 1991.
[2] K. Binder (Ed.), Monte Carlo and Molecular Dynamics Simulatons in Polymer Science, Oxford University Press, Oxford, 1995.
[3] G.D. Smith, D.Y. Yoon, J. Chem. Phys. 100 (1994) 649.
[4] G.D. Smith, D.Y. Yoon, W. Zhu, M. Ediger, Macromolecules 28 (1995) 5897.
[5] W. Paul, D.Y. Yoon, G.D. Smith, J. Chem. Phys. 103 (1995) 1702.
[6] W. Paul, G.D. Smith, D.Y. Yoon, Macromolecules 30 (1997) 7772.
[7] G.D. Smith, W. Paul, D.Y. Yoon, A. Zirkel, J. Hendricks, D. Richter, H. Schober, J. Phys. Chem. 107 (1997) 4751.
[8] M. Mondello, G.S. Grest, J. Chem. Phys. 106 (1997) 9327.
[9] W. Paul, G.D. Smith, D.Y. Yoon, B. Farago, S. Rathgeber, A. Zirkel, L. Willner, D. Richter, Phys. Rev. Lett. 57 (1998) 843.
[10] M. Mondello, G.S. Grest, E.B. Webb III, P. Peczak, J. Chem. Phys. 109 (1998) 798.
[11] D. Richter, B. Ewen, B. Farago, T. Wagner, Phys. Rev. Lett. 62 (1989) 2140.
[12] G.D. Smith, W. Paul, M. Monkenbusch, L. Willner, D. Richter, X.H. Qiu, M.D. Ediger, Macromolecules 32 (1999) 8857.
[13] D. Richter, B. Farago, L.J. Fetters, J.S. Huang, B. Ewen, C. Lartigue, Phys. Rev. Lett. 64 (1991) 1389.
[14] D. Richter, R. Butera, L.J. Fetters, J.S. Huang, B. Farago, B. Ewen, Macromolecules 25 (1992) 6156.
[15] D. Richter, L. Willner, A. Zirkel, B. Farago, L.J. Fetters, J.S. Huang, Phys. Rev. Lett. 71 (1993) 4158.
[16] P. Schleger, B. Farago, C. Lartigue, A. Kollmar, D. Richter, Phys. Rev. Lett. 81 (1998) 124.
[17] B. Frick, D. Richter, W. Petry, U. Buchenau, Z. Phys. B 70 (1988) 73.
[18] D. Richter, B. Frick, B. Farago, Phys. Rev. Lett. 61 (1988) 2465.
[19] B. Frick, B. Farago, D. Richter, Phys. Rev. Lett. 64 (1990) 2921.
[20] R. Zorn, D. Richter, B. Frick, B. Farago, Physica A 201 (1993) 52.
[21] B. Frick, D. Richter, Science 267 (1995) 1939.
[22] R. Zorn, A. Arbe, J. Colmenero, B. Frick, U. Buchenau, Phys. Rev. E 52 (1995) 782.
[23] A. Arbe, U. Buchenau, L. Willner, D. Richter, B. Farago, J. Colmenero, Phys. Rev. Lett. 76 (1996) 1872.
[24] A. Arbe, D. Richter, J. Colmenero, B. Farago, Phys. Rev. E 54 (1996) 3853.
[25] D. Richter, J. Phys.: Condens. Matter 8 (1996) 9177.
[26] D. Richter, A. Arbe, J. Colmenero, M. Monkenbusch, B. Farago, R. Faust, Macromolecules 31 (1998) 1133.
[27] D. Richter, M. Monkenbusch, J. Allgeier, A. Arbe, J. Colmenero, B. Farago, Y.C. Bae, R. Faust, J. Chem. Phys. 111 (1999) 6107.
[28] S. Nosé, J. Chem. Phys. 81 (1984) 511.
[29] M.Doi, S.F. Edwards, The Theory of Polymer Dynamics, Cornell University Press, Ithaca, 1979.
[30] D.A. McQuarrie, Statistical Mechanics, Harper and Row, New York, 1976.
[31] G.D. Smith, W. Paul, J. Phys. Chem. A 102 (1998) 1200.
[32] M.E. Tuckerman, D.J. Tobias, M.L. Klein, G. Martyna, Mol. Phys. 87 (1996) 1117.
[33] W. Paul, K. Binder, D.W. Heermann, K. Kremer, J. Chem. Phys. 95 (1991) 7726.
[34] A. Kopf, B. Dünweg, W. Paul, J. Chem. Phys. 107 (1997) 6945.
[35] M. Guenza, J. Chem. Phys. 110 (1999) 7574.
[36] P.E. Rouse, J. Chem. Phys. 21 (1955) 1273.
[37] A. Kolinski, J. Skolnick, R. Yaris, J. Chem. Phys. 86 (1987) 1567.
[38] A. Kolinski, J. Skolnick, R. Yaris, J. Chem. Phys. 86 (1987) 7164.
[39] W. Paul, K. Binder, D.W. Heermann, K. Kremer, J. Chem. Phys. 95 (1991) 7726.
[40] K. Okun, M. Wolfgardt, J. Baschnagel, K. Binder, Macromolecules 30 (1997) 3075.

[41] A. Kopf, B. Dünweg, W. Paul, J. Chem. Phys. 107 (1997) 6945.
[42] L. Harnau, R.G. Winkler, P. Reineker, J. Chem. Phys. 104 (1996) 6355.
[43] L. Harnau, R.G. Winkler, P. Reineker, Phys. Rev. Lett. 82 (1999) 2408.
[44] G. Allegra, F.J. Ganazzoli, J. Chem. Phys. 74 (1981) 1310.
[45] G. Allegra, F.J. Ganazzoli, Macromolecules 14 (1981) 1110.
[46] W. van Megen, T.C. Mortensen, S.R. Williams, J. Müller, Phys. Rev. E 58 (1998) 6073.